#### **RESEARCH ARTICLE**



# High-speed lava flow infrasound from Kīlauea's fissure 8 and its utility in monitoring effusion rate

John J. Lyons<sup>1</sup> · Hannah R. Dietterich · Matthew P. Patrick · David Fee<sup>3</sup>

Received: 21 June 2021 / Accepted: 27 August 2021
This is a U.S. government work and not under copyright protection in the U.S.; foreign copyright protection may apply 2021

#### Abstract

The 2018 eruption of Kīlauea Volcano produced large and destructive lava flows from the fissure 8 (Ahu 'aila 'au) vent with flow velocities up to 17 m s<sup>-1</sup>, highly variable effusion rates over both short (minutes) and long (hours) time scales, and a proximal channel or spillway that displayed flow features similar to open channel flow in river systems. Monitoring such dynamic vent and lava flow systems is a challenge. Our results demonstrate that infrasound, combined with ground-based observations and imagery from unoccupied aircraft systems (UAS), can be used to distinguish vent degassing activity from high-speed lava flow activity. We use spectral characteristics and the infrasound frequency index (FI) to distinguish spillway infrasound from vent infrasound. Comparing FI with flow speeds derived from UAS videos reveals that spillway infrasound only occurs when flow speeds were sufficiently high to cause a supercritical flow state and breaking waves (Froude values > 1.7), and we propose that the spillway signals are produced primarily through the interaction of the turbulent lavafree surface with the atmosphere. We show that FI can also provide a means to track bulk effusion rate. Our results indicate that infrasound offers a new way to characterize lava flow channel hydraulics and is a powerful tool for monitoring effusive eruptions when high-speed flows are possible.

**Keywords** Infrasound · Lava effusion rate · Supercritical flow · Eruption monitoring · Kīlauea volcano

#### Introduction

High-speed lava flows present a monitoring and research challenge. Channelized flows with low viscosities can reach speeds over 10 m s<sup>-1</sup> (Lipman and Banks 1987; Baloga et al. 1995; Geist et al. 2008; Patrick et al. 2019; Dietterich et al. 2021). These flows are capable of delivering large volumes

Editorial responsibility: G.P. Waite

Published online: 05 October 2021

This paper constitutes part of a topical collection:

The historic events at Kilauea Volcano in 2018: summit collapse, rift zone eruption, and Mw6.9 earthquake

- ☑ John J. Lyons jlyons@usgs.gov
- U.S. Geological Survey, Alaska Volcano Observatory, Alaska, Anchorage, USA
- U.S. Geological Survey, Hawaiian Volcano Observatory, Hawaii, Hilo, USA
- Geophysical Institute, Alaska Volcano Observatory, University of Alaska Fairbanks, Fairbanks, AK, USA

of lava to populated areas at significant distances from the source, which can produce extensive damage to infrastructure and long-lasting disruptions to local communities (Tedesco et al. 2007; Neal et al. 2019). Monitoring effusion rate for potentially hazardous changes in flux has typically relied on close-range, ground-based methods (Lipman and Banks 1987; Slatcher et al. 2015) or estimations using satellite thermal imagery (Harris and Baloga 2009; Vicari et al. 2011). Recent applications have also used proximal remote sensing with ground-based time-lapse imagery and video from unoccupied aircraft systems (UAS) to track effusion rate with flow speed and depth (Patrick et al. 2019; Dietterich et al. 2021). These methods can provide detailed and accurate measurements, but not real-time flux information needed for continuously updating flow models and hazard maps. The ability of geophysical methods to provide continuous, high-sample rate observations at safe distances motivates ongoing research into detection and characterization of mass flows (Allstadt et al. 2018), including into infrasound from lava flows.

Infrasound data are increasingly utilized to monitor and study a wide range of mass surface flows, including snow and ice avalanches (Ulivieri et al. 2011; Marchetti et al.



2015; Toney et al. 2021), debris flows (Schimmel and Hübl 2016; Marchetti et al. 2019), lahars (Johnson and Palma 2015), pyroclastic flows (Ripepe et al. 2010), and fluvial processes (Schmandt et al. 2013; Ronan et al. 2017). Observations of lava flow infrasound, however, are limited. Garcés et al. (2003a) observed 1-10-Hz tremor during lava effusion in a tube system at Kīlauea's Pu 'u 'Ō 'ō crater in 2002 and attributed the signal to possible cavity resonance in the extended tubes or to fluid flow instabilities. Infrasound was also detected from a skylight in 2007 Pu 'u 'Ō 'ō lava tube flows, indicating that variable degassing can occur downstream from vents (Matoza et al. 2010). Lava flow velocities are typically highest adjacent to vents (Lipman & Banks, 1987) that are sources of energetic infrasound themselves and have been the focus of other studies (Fee et al. 2011: Patrick et al. 2019), leaving outstanding questions about the character and detectability of lava flow infrasound, as well as its potential utility in flow monitoring.

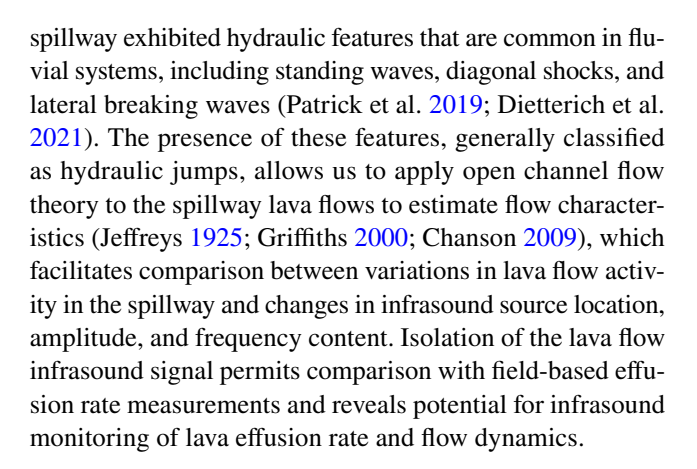
66

Channelized lava flows share features with open channel flow in river systems, including hydraulic jumps, that aid in determining flow parameters that are difficult to directly measure (Griffiths 2000; Le Moigne et al. 2020; Dietterich et al. 2021). Hydraulic jumps are waves that form where supercritical flow transitions to subcritical flow (Chanson, 2009), but not all jumps are sufficiently energetic to be sources of detectable infrasound. The critical state of flow in a Newtonian fluid is defined by the dimensionless Froude number (Fr) (Chow 1959):

$$Fr = \frac{v}{\sqrt{gd}} \tag{1}$$

where v = mean flow velocity, d = flow depth, and g = gravitational acceleration. The flow state is critical when Fr = 1, subcritical when Fr < 1, and supercritical when Fr > 1. A flow in a supercritical state will produce a hydraulic jump whenever the flow or channel characteristics are favorable. Ronan et al. (2017) studied controlled fluvial hydraulic jumps and found that infrasound began to be produced when waves transitioned from nonbreaking undular jumps to breaking weak jumps at Fr values above 1.7. Similar results were observed in seismoacoustic data from whitewater river rapids (Schmandt et al. 2013). These observations and the similarity between fluvial systems and high-speed lava flows suggest that lava flows under certain conditions likely produce infrasound, although detecting and isolating what may be weak signals from other sources (i.e., vents) may be challenging.

This study investigates infrasound generated from Kīlauea's 2018 fissure 8 vent (Ahu 'aila 'au) and its proximal high-speed lava flow channel, or spillway, in order to determine the characteristics of lava flow infrasound and distinguish it from vent infrasound. The fissure 8 lava flow



# The 2018 Kīlauea eruption: pulses and surges in effusion rate

The 2018 lower East Rift Zone (LERZ) eruption that began on 3 May 2018 produced the most destructive Hawaiian lava flows in the past 200 years (Neal et al. 2019). The LERZ eruption lasted 3 months with activity spread over 24 separate fissure vents. Fissure 8 was the longest-lived vent and produced lava fountaining and a large channelized lava flow (Fig. 1) from 28 May to 4 August that was responsible for more than 90% of the total erupted volume (Gansecki et al. 2019; Dietterich et al. 2021). The longevity and relative stability of the fissure 8 vent and proximal flow channel allowed it to be extensively monitored with both ground-based and remote sensing techniques (Zoeller et al. 2018; Neal et al. 2019). Activity at fissure 8 during the study period was dominated by low fountaining (20- to 80-m) at the vent that fed lava into a proximal channel, or spillway, that was 30-m wide and 300-m long extending north from the vent with an average gradient of 1.5 (Fig. 1; Patrick et al. 2019). This channel widened downslope and fed a lava flow that extended 13 km to the ocean.

Field crews observed two types of cyclic variations in eruptive activity at fissure 8 starting in mid-July: short-term variations termed pulses and long-term variations termed surges (Patrick et al. 2019). Both pulses and surges resulted in changes in infrasound source back-azimuths away from the vent and toward the spillway (Fig. 2c), suggesting the potential for lava flow infrasound during these events. Pulses produced rapid changes in the speed and level of lava in the spillway over 6–10-min cycles that lasted from 1 to 18 h. Analysis of ground-based video data of pulses shows lava flow velocities of 4–5 m s<sup>-1</sup> during the low flow stage of cycles that increased to 12–17 m s<sup>-1</sup> during the high flow stage of the cycles as the lava level in the channel rose by several meters (Patrick et al. 2019). The video pulse measurements were used to calculate bulk effusion rates for some pulses, which varied from ~350  $m^3$  s<sup>-1</sup> in the pulse troughs to ~ 1700 m<sup>3</sup> s<sup>-1</sup> at the pulse peaks.



Bulletin of Volcanology (2021) 83:66 Page 3 of 12 6



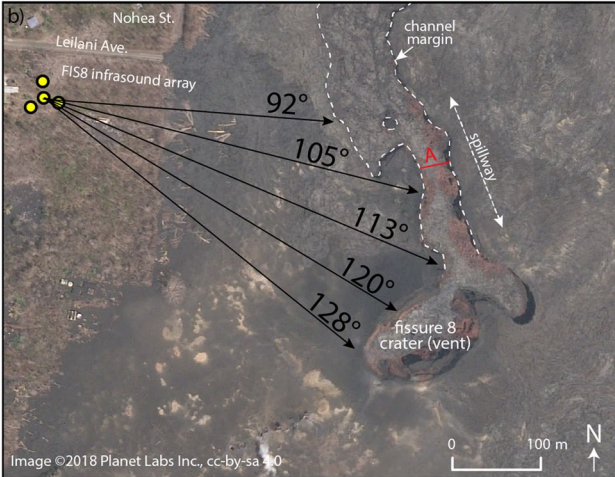


**Fig. 1** Fissure 8 vent and channel geometry modified after Patrick et al. (2019). (a) Aerial image looking east showing the vent, spillway, and distal flow of fissure 8 on 29 July 2018. (b) Post-eruption satellite image showing the location of the infrasound array with respect to the fissure 8 vent and spillway. Black rays indicate the back-azimuths from the end of the spillway to the southwest edge of the vent. Red line "A" indicates location of ground-based and UAS flow measurements. Image courtesy of Planet Labs

Unoccupied aircraft systems (UAS) also captured a video during pulse sequences that was analyzed to infer lava flow parameters including velocity, depth, and viscosity (Dietterich et al. 2021).

Surges were much longer-duration increases in lava fountain and flow activity that closely followed collapse events at the summit crater of Kīlauea, 40 km uprift from fissure 8, that occurred every 25 to 50 h (Patrick et al. 2019). Video data from the spillway show that the lava level began to rise as soon as 13 min after a collapse on 31 July, with levels typically peaking 2–3 h after summit collapses. Effusion rate estimates from video data of four collapses in late July and early August reveal that pre-collapse bulk effusion rates were 300–700

m<sup>3</sup> s<sup>-1</sup> and increased to peaks of 1400–1700 m<sup>3</sup> s<sup>-1</sup> within 4 h of collapses (Patrick et al. 2019).

#### **Data and methods**

The infrasound data analyzed in this study are from a 4-element campaign array installed on 4 June 2018 that ran nearly continuously through the end of the LERZ eruption. The FIS8 array was equipped with Chaparral Physics model 60-UHP sensors (sensitivity 0.009 v/ Pa and flat response 0.03-245 Hz) connected to DiGOS DATA-CUBE digitizers sampling at 400 Hz. The array aperture was 36 m, and it was located 450 m northwest of the fissure 8 vent (Fig. 1). We calculated a theoretical uncertainty in back-azimuth of 3–4° for the array geometry using the method of Szuberla and Olson (2004). Sensor locations from handheld GPS receivers were found to be inaccurate due to thick tree cover, resulting in spurious array processing results. We instead used locations from the digitizer GPS and averaged the locations over thousands of measurements.

Here, we outline the infrasound array processing steps and the methods used to distinguish and characterize signals originating from the fissure 8 vent from those originating along the spillway. The infrasound array data were processed to identify coherent signals using a least-squares beamforming algorithm (Olson and Szuberla 2005). Continuous waveforms were processed in 10-s windows (unless otherwise noted) with 50% overlap. Signals are considered to have originated from the fissure 8 vent and spillway if the source back-azimuth is between 90 and 130° (Fig. 1), the mean cross-correlation maximum (MCCM) between sensor pairs is greater than 0.5, and the trace velocity is 300–400 m s<sup>-1</sup>. The frequency distribution of signals from the fissure 8 – spillway area is quantified by computing the power spectral density (PSD) of the beamformed waveform. The relative infrasound energy  $(E_{ac})$  in each window is calculated by integrating the squared pressure over time (Fee et al. 2013):

$$E_{\rm ac} = \int_0^T \Delta p^2(t) dt \tag{2}$$

We are using a relative measure of infrasound energy because other investigations of the fissure 8 infrasound indicate that jet noise contributes significantly to the infrasonic wavefield (Gestrich et al., in review). Thus, simple spherical radiation cannot be assumed and any measure of energy or intensity on this one array will be relative to this array. Characterizing the absolute infrasound energy radiated would require observations from multiple arrays, potentially at different elevations to the source (Matoza et al. 2013).



66 Page 4 of 12 Bulletin of Volcanology (2021) 83:66

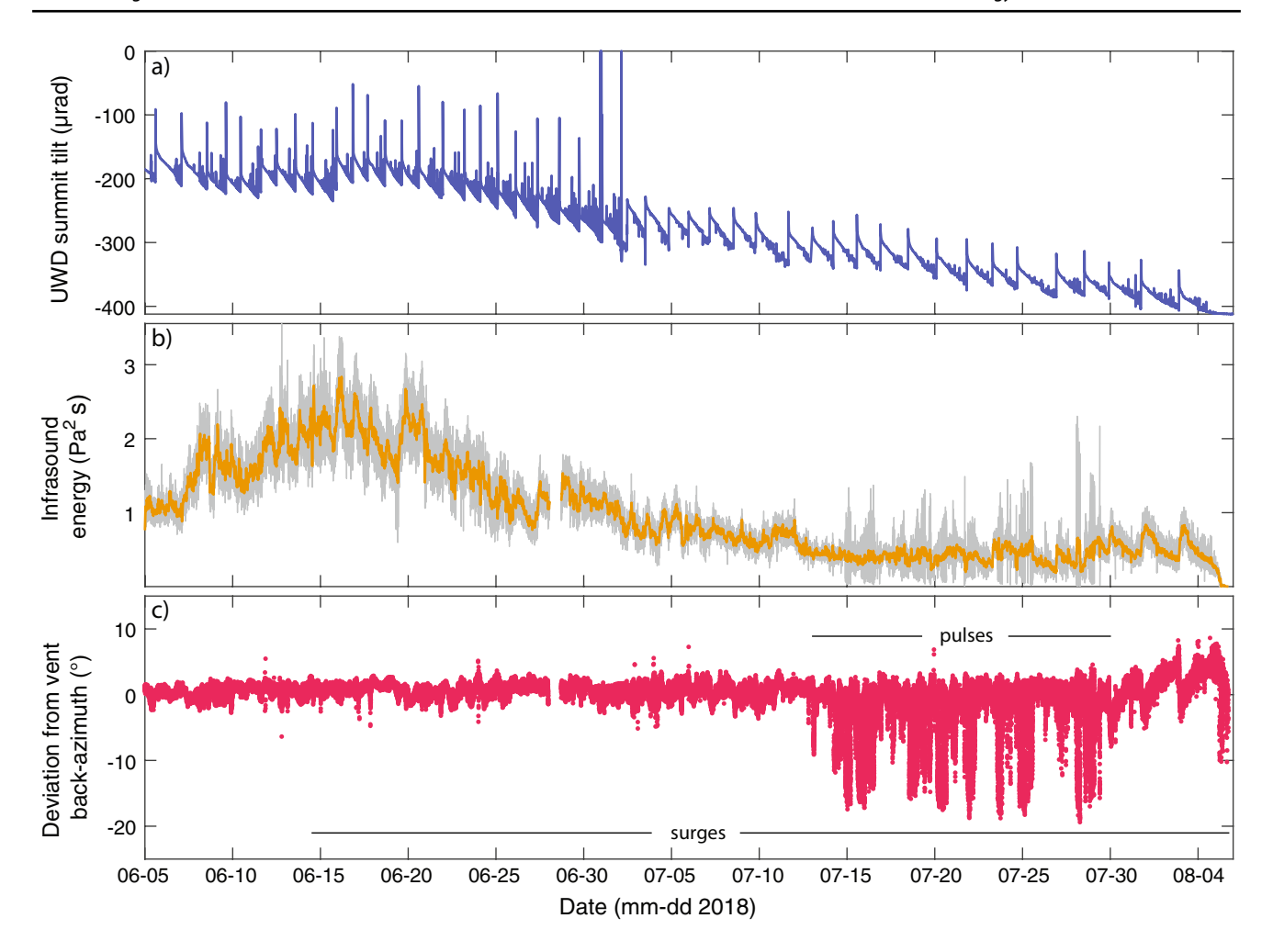


**Fig. 2** Overview of Kīlauea summit tilt and LERZ infrasound from fissure 8. (a) Tilt data from summit station UWD showing quasi-periodic signals caused by collapses in the floor of the Halema 'uma 'u crater. (b) Infrasound energy from beamformed array data (30-s windows in gray and 30-min RMS-averaged values in orange). The short

gap in late June is due to a power outage at the array. (c) Infrasound source back-azimuth shown in degrees of deviation from the fissure 8 vent (121°). Also shown are the approximate durations of the two types of cyclic variations in effusion rate observed at fissure 8: pulses (short-duration) and surges (long-duration)

We use the frequency index of Buurman and West (2010) on infrasound signals from fissure 8 and the spillway to investigate changes in signal frequency through time. The frequency index (FI) is calculated as:

$$FI = \log_{10} \frac{A_{\text{upper}}}{A_{\text{lower}}}$$
 (3)

where  $A_{\rm upper}$  is the mean spectral amplitude in an upper band of frequencies and  $A_{\rm lower}$  is the mean spectral amplitude in a lower band of frequencies. The  $A_{\rm lower}$  range used here is 0.4–6 Hz and the  $A_{\rm upper}$  range is 6–20 Hz. These values were determined by reviewing PSD curves of signals from the vent and spillway, and with the lower cutoff set to reduce microbarom noise and the upper cutoff set to reduce noise from frequent helicopter overflights. Frequency index values

are only calculated on the beamformed trace when the array processing thresholds are met for a signal originating from the fissure 8 – spillway area (Fee et al. 2020).

The nondimensional Froude value establishes the critical state of flow through time for periods when UAS video captured pulsing events. We calculate the Froude value of the lava flows using Eq. 1 during pulse sequences captured in UAS video (Dietterich et al. 2021) at the location shown in Fig. 1b. UAS video frames were extracted at 8–10 frames/s when the UAS was in a stable hover and the lava flows were not obscured by fume. Maximum surface velocity was calculated at fixed channel cross sections by comparing adjacent frames. A median filter with a 5-s window was used on the flow velocity data during pulses (see Dietterich et al. 2021, for UAS and video details). The depths of the lava flows were calculated using shallow water flow theory (Jeffreys 1925), with



Bulletin of Volcanology (2021) 83:66 Page 5 of 12 6

flow velocity and underlying slope data and rheological properties of lava samples collected near the vent (Jeffreys 1925; Dietterich et al. 2021).

#### Results

### **Fissure 8 infrasound characteristics**

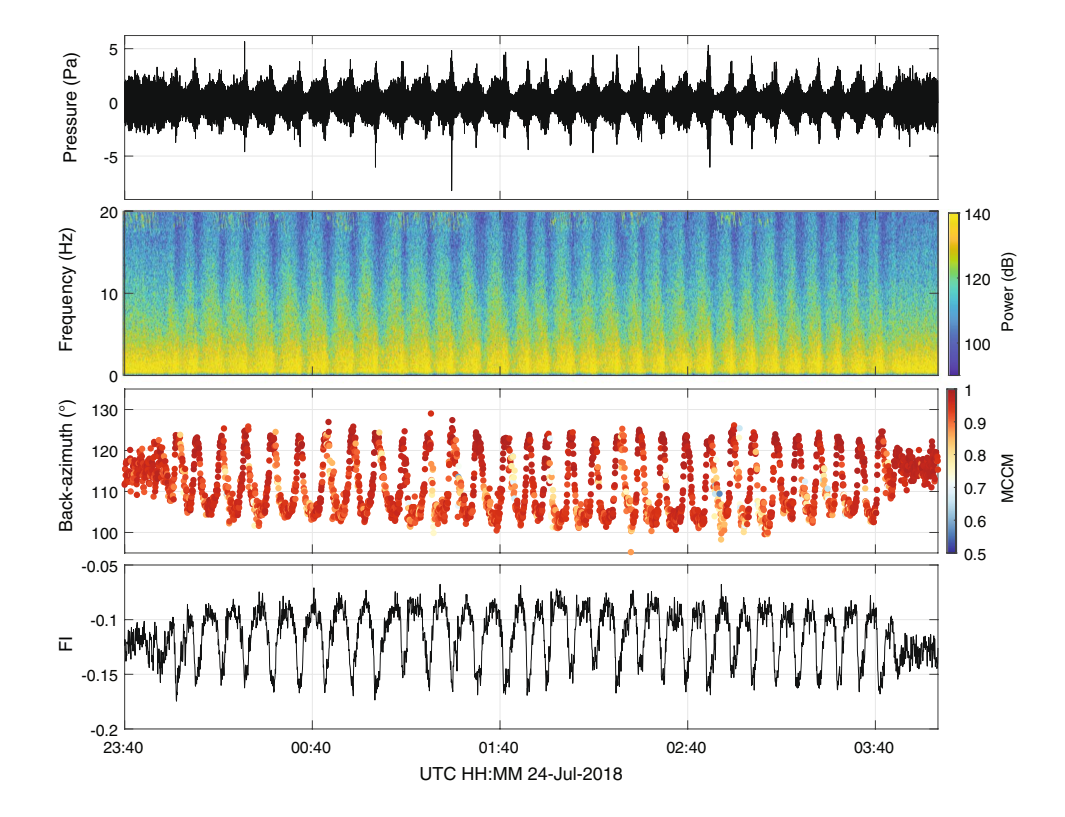
An overview of the FIS8 infrasound array data from fissure 8 is shown in Fig. 2 along with tilt data from the Kīlauea summit station UWD that indicate the timing of the caldera collapses. The array data were filtered from 0.4 to 20 Hz, beamformed, and array processed using 60-s windows with 50% overlap. Infrasound energy increased rapidly in early June shortly after the array was installed, and 9 days after activity focused at fissure 8 on May 28 (Dietterich et al. 2021). Energy levels peaked in mid-June and then slowly declined and leveled off from mid-July until the end of the eruption. The 30-s energy values generally track the 30-min smoothed energy values, except during the pulsing behavior when the largest short-term swings in amplitude are seen (Fig. 2b). Increases in infrasound energy following summit collapses can be seen as a sawtooth pattern in the 30-min RMS energy data starting as early as June 11 and are especially clear following the last few collapses of the eruption. Field crews began reporting surges in lava effusion following summit collapses in late June, but an outstanding question concerns whether the earlier increases in infrasound energy following collapses were also accompanied by increases in effusion rate or changes in lava fountain activity.

The fissure 8 vent and associated lava fountain were an almost uninterrupted source of coherent infrasound from the beginning of the dataset until the onset of field crew reports about short-term cycles in effusion rate (pulses) in mid-July. The infrasound back-azimuth from each time window, measured in degrees from the center of the fissure 8 vent (121°), is depicted in Fig. 2c. The infrasound back-azimuth was fixed steadily on the vent with just minor variations of a few degrees until pulses began in the middle of July. Once pulses began, large (20°+) variations in back-azimuth were recorded as the dominant infrasound source moved from the fissure 8 vent, down the spillway, and then back to the vent during each pulse cycle. The longer-term surges also produced changes in the source back-azimuth toward and in some cases down the spillway following summit collapses. These changes were generally smaller than those produced by pulses or are obscured by pulse sequences in mid-July. The clearest changes in back-azimuth associated with surges occur following the final four summit collapses.

# Pulse infrasound and frequency index

The short-term pulses in effusion rate from fissure 8 generated remarkable infrasound signals that are unique across

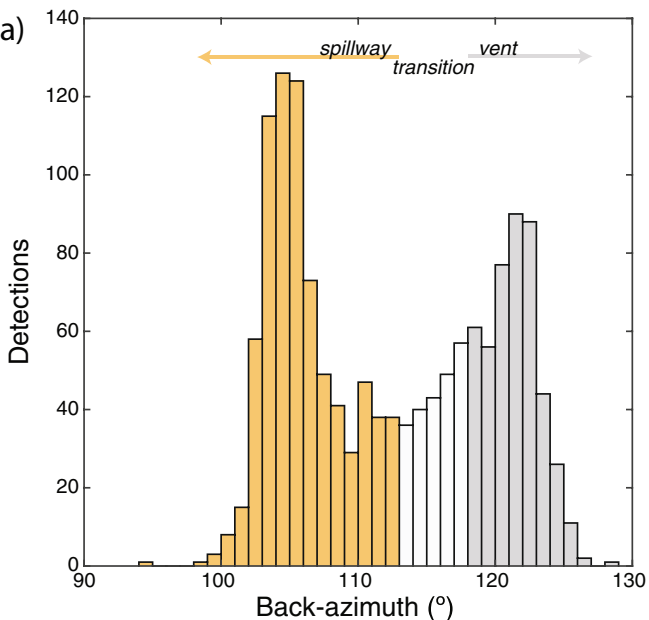
Fig. 3 Fissure 8 pulse sequence example. (a) Infrasound waveform, (b) frequency spectrogram, (c) back-azimuth, and (d) FI values for a typical pulse sequence lasting 4 h on July 24–25





the eruption sequence in both amplitude and back-azimuth. Pulse sequences produced the largest short-term variations in amplitude of the entire data set, as well as the largest variations in back-azimuth. At the onset of a pulse sequence, the amplitude would begin to vary higher and lower than the steady amplitude prior to pulsing (Fig. 3). The variation in amplitude corresponded with changing back-azimuths as the dominant source of coherent infrasound moved from the fissure 8 vent to sources along the spillway (Fig. 3). The vent source always produced the highest amplitude signals during each pulse sequence. During each 6–10-min pulse, the vent source would only remain active for 1-2 min followed by infrasound emissions further down the spillway. The lowest amplitude infrasound typically occurred after peak amplitude in the 1–2-min transition between vent and spillway sources as the back-azimuths progressively swept down the spillway (Fig. 3). Amplitudes would begin increasing as spillway signals became stronger, with back-azimuths indicating sources at or near the maximum distance down the spillway. The distal spillway source would persist for 2-4 min with steady or slightly increasing amplitude until the sources began to sweep back up the spillway to return to the vent over 1-2 min. The pulse sequences sometimes only contained a few cycles, but more often would continue for hours with only subtle changes in amplitude and backazimuth (Fig. 3). The longest pulse sequence lasted more than 18.5 h on July 15-16.

Analysis of UAS videos showed that the morphology of the fissure 8 vent and spillway channel was essentially unchanged during the pulsing episodes (Desmither et al. 2021; Dietterich et al. 2021). This allowed us to characterize the difference between the vent and spillway sources based on infrasound frequency content. We assigned vent source back-azimuths from 118 to 130° and spillway source back-azimuths from 90 to 113° (Fig. 1). Signals between 113 and 118° spanned the area at the edge of the vent as it moved into the spillway, and we term this source region the transition (Fig. 4a). The distribution of sources in pulse sequences often showed a bimodal distribution, with a peak in detections at a vent location (~121-123°) and another peak at a mid-spillway location (~103–105°) (Fig. 4a). The frequency content of spillway and vent sources is somewhat similar, and since the sources were adjacent and partially overlap temporally, identifying differences in individual PSD curves is challenging. However, we find that stacking PSD curves from spillway and vent sources over hours-long pulse sequences reveals clear differences in the frequency content of vent and spillway sources (Fig. 4b). Vent sources were enriched in lower frequencies compared to spillway sources while spillway sources contained more higher frequency energy than the vent sources. The vent and spillway PSD curves intersect around 6 Hz, and we use this value to separate the upper and lower bands when calculating the FI.



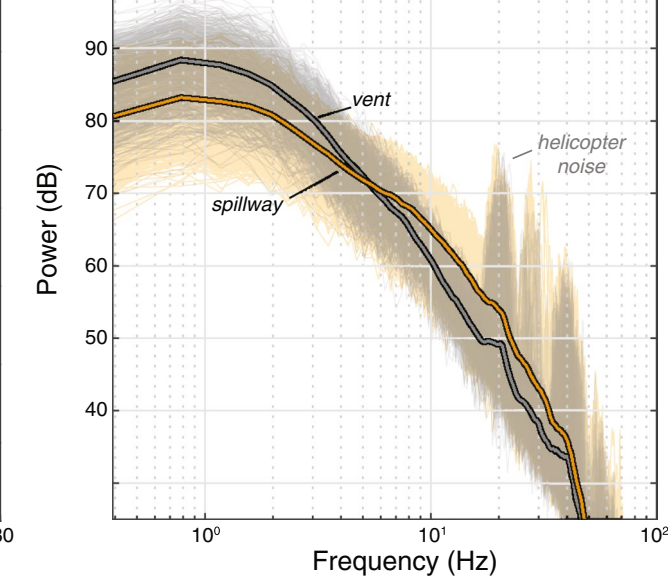


Fig. 4 Back-azimuth and frequency content of pulse sequence from Fig. 3. (a) Histogram of back-azimuths with a clear bimodal distribution between spillway and vent sources. The range of back-azimuths assigned to the spillway, vent, and transition areas is based on analysis of UAS imagery (Fig. 1). (b) PSD curves for vent and spillway

sources from (a). PSD curves were calculated for each array processing window and then stacked to produce the aggregate vent (gray) and spillway (orange) curves. The distinct peaks in some of the individual curves at 20 Hz and higher are noise due to helicopter overflights



Bulletin of Volcanology (2021) 83:66 Page 7 of 12 66

The FI values for pulse events provide a simple means of confirming that the vent and spillway sources are distinct, not simply the same infrasound-generating process operating at the vent and in the spillway. As a time series, the FI values offer timing constraints on the relative contribution of the spillway and vent sources to the infrasound signals. The FI time series also complements the source back-azimuth time series that together highlight the periodic change in source location and character during each pulse cycle (Fig. 3c). FI is nearly a mirror image of the back-azimuth results with the highest FI values corresponding with well-correlated, high-amplitude spillway signals and the lowest FI values tracking with the highest-amplitude vent signals.

#### **Discussion**

#### Infrasound from a lava flow

The open channel flow features generated repeatedly by the spillway lava flows during pulse cycles are capable of producing infrasound in fluvial settings (Schmandt et al. 2013; Ronan et al. 2017), prompting our investigation into whether the spillway source identified in the FI data is generated by the lava flow directly or through some other associated process like enhanced degassing. UAS videos of the spillway and vent area during pulses provide high sample rate flow measurements to compare with the infrasound data (Dietterich et al. 2021). The flow data derived from the UAS videos is limited in duration

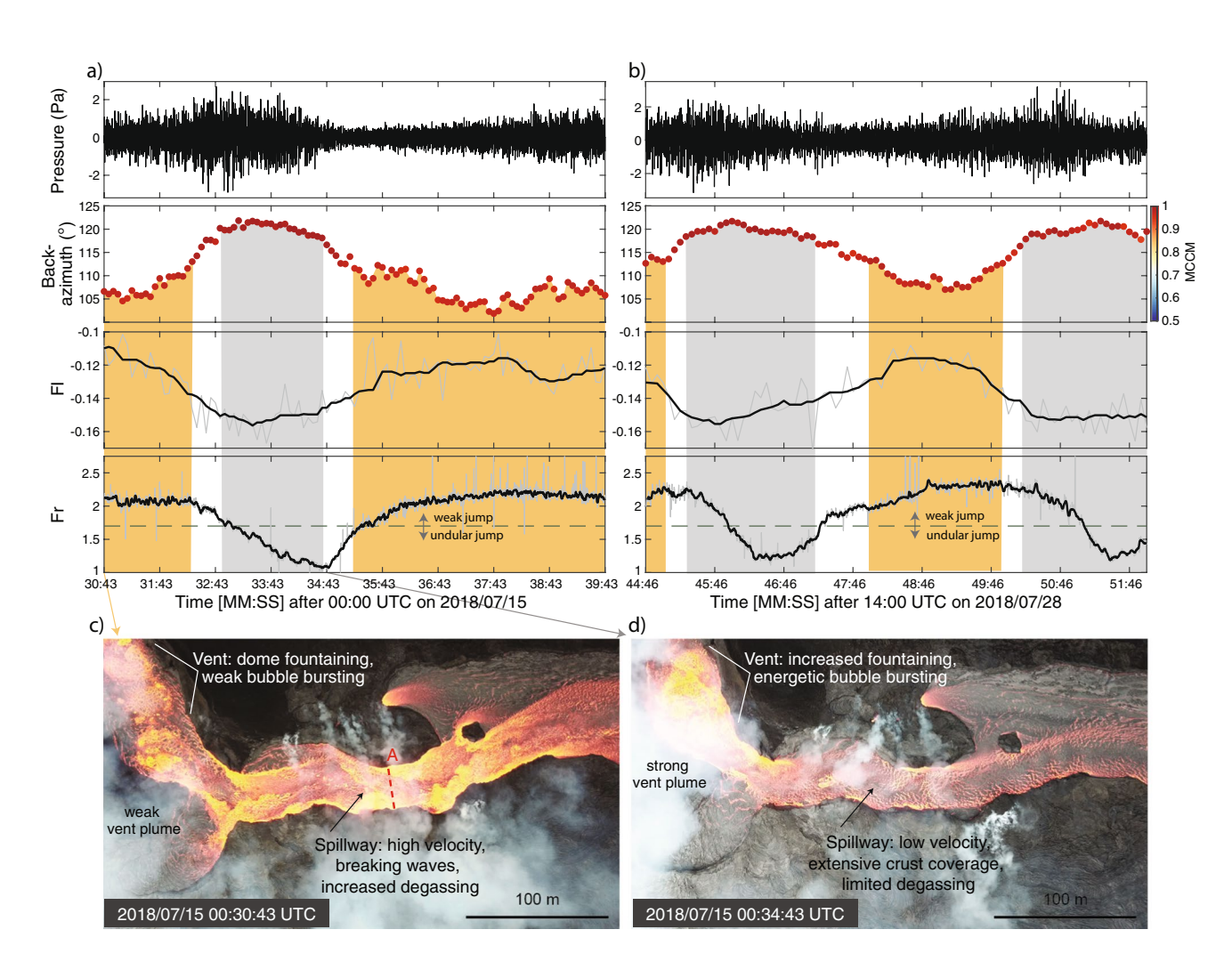


**Fig. 5** Infrasound and UAS-derived lava flow data from two pulse cycles. Both (a) and (b) show, in descending order, pressure waveform, source back-azimuth, FI, and Fr values. Faint gray line shows full sample rate FI and Fr values. The overlying black line is the same data with a 10th order median filter applied. Background colors on the bottom three panels indicate assumed infrasound source locations, as in Fig. 4 (orange=spillway, white=transition, gray=vent).

Dashed line in bottom plot at Fr = 1.7 indicates where a non-breaking jump transitions to a breaking weak jump. Fluvial standing waves have been shown to generate coherent infrasound at values above Fr = 1.7 (Ronan et al. 2017). (c and d) Frames from UAS videos during pulse cycle shown in (a). Images highlight the variations in vent and spillway activity during (c) spillway-dominated infrasound and (d) vent-dominated infrasound



by the flight time; thus, videos capturing full pulse cycle videos are rare. The magnitudes of the Fr values calculated for the two pulse cycles shown in Fig. 5 correspond closely to the FI values. There is a ~ 1-min delay or offset between key peaks and troughs in the Fr values compared to the FI data that we attribute to the time for the transition to propagate from the vent to the velocity measurement location ~ 100 m down the spillway. Fr values approach minimums near 1 when FI values are lowest, and backazimuths indicate a vent source (Fig. 5). Maximum Fr values occur when FI values are highest, and back-azimuths indicate a spillway source. Ronan et al. (2017) found that fluvial waves begin to produce detectable infrasound at Fr = 1.7, when a standing wave transitions from a undular (non-breaking) hydraulic jump to a breaking weak jump. Using this value as a guide indicates that Fr values associated with spillway sources are always > 1.7, while vent sources are < 1.7 (Fig. 5) or are decreasing from higher spillway values toward values < 1.7.

The primary mechanism of infrasound generation in fluvial systems is thought to be interactions at the fluid - air interface as waves begin to break (Schmandt et al. 2013; Ronan et al. 2017). Breaking ocean waves have also been associated with infrasound generation (e.g., Arrowsmith and Hedlin 2005; Aucan et al. 2006; Garcés 2003b; Lyons et al. 2014). Breaking wave features consistent with Fr values greater than 1.7 were routinely seen in the spillway during pulse sequences (Patrick et al. 2019; Dietterich et al. 2021). The waves typically developed first along the upper reaches of the spillway and progressively advanced further down the spillway as effusion rate in each pulse cycle increased (Online Resource 1). An especially vigorous set of lateral breaking waves often formed near the "A" line in Figs. 1 and 5c and corresponds with the region of lowest back-azimuth values observed during pulses (Fig. 5, Online Resource 1). The correlation between FI and Fr and the observed breaking waves in the spillway support an interpretation that the spillway infrasound signals were primarily generated by lava – air interactions when lava flow speeds increased to the point at which the flow became supercritical, or at about 10 m s<sup>-1</sup> for the fissure 8 lavas. An additional consideration is that the lava, unlike water in fluvial systems, was actively degassing in the spillway and could be an additional source of infrasound. Enhanced degassing along the spillway during peaks in effusion rate associated with pulses was reported by field teams and is evident in UAS imagery (Fig. 5, Online Resource 1). The spillway degassing appears to be diffuse and occurred along most of the length of the spillway, likely enhanced by agitation of the flow surface and breaking waves (Fig. 5, Online Resource 1). If the spillway infrasound was primarily due to degassing rather than breaking waves, the frequency content of the spillway signal would likely be more similar to the vent infrasound that is attributed to focused, energetic degassing, and would be unlikely to produce the correlation between FI and Fr values. Future work comparing lava flow infrasound to infrasound from fluvial systems may permit a more thorough understanding of how much diffuse lava degassing might contribute to the spillway infrasound.

### Infrasound as a proxy for lava effusion rate

Monitoring effusion rate at high-volume, high-speed flows like fissure 8 is essential for hazard assessment and operational monitoring but real-time, high-sample rate tools are limited. Based on the positive correlation between FI and UAS-derived Fr values, we also calculated FI values to compare with bulk effusion rate estimates during pulse and surge activity. Bulk effusion rate estimates were made from ground-based video and time-lapse imagery at 10-s intervals during pulsing on July 14–15 and at 30–60-s intervals during surges with no pulsing on July 29 and 31 and August 2 (Patrick et al. 2019). The hours-long ground-based effusion rate estimates capture more varied activity than the shorter UAS-derived video and provide a more comprehensive dataset for investigating the relationship between effusion rate and both infrasound amplitude (energy) and FI.

The July 14–15 pulse data reveals a weak anticorrelation (R = -0.23) between bulk effusion rate and infrasound energy but a strong positive correlation (R = 0.74) between bulk effusion rate and FI (Fig. 6). These correlations also correspond to infrasound back-azimuth source locations, with higher effusion rates, lower infrasound energy, and higher FI associated with spillway sources and lower effusion rates, higher infrasound energy, and lower FI corresponding with vent sources. The anticorrelation between effusion rate and infrasound energy during pulses was reported by Patrick et al. (2019), who saw a similar trend in real-time seismic amplitude measurements (RSAM) from the station nearest fissure 8. They attribute the anticorrelation between infrasound and seismic amplitude and effusion rate to variations in outgassing at the vent. When outgassing was vigorous at the vent, higher infrasound and seismic amplitudes were observed, as well as low effusion rates and flow velocities in the spillway. When vent degassing waned, flow velocity increased, more diffuse degassing occurred in the spillway, and infrasound and seismic amplitudes were reduced. The infrasound FI data build on these observations by allowing the contributions of both the vent and spillway sources to be represented and compared together with effusion rate, resulting in a strong correlation rather than a weak anticorrelation.

The surge data show a positive correlation between bulk effusion rate and both infrasound energy and FI, although FI shows a stronger correlation for the July 31 surge and



Bulletin of Volcanology (2021) 83:66 Page 9 of 12 66

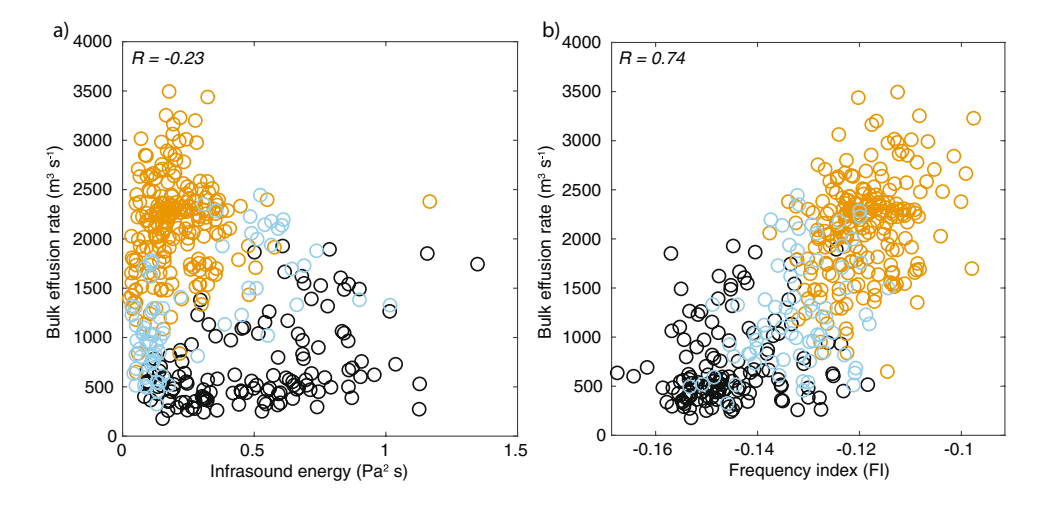


**Fig. 6** Lava effusion rate compared with infrasound energy and frequency index during the July 14–15 pulse sequence. Bulk effusion rate data from Patrick et al. (2019). (a) Bulk effusion rate shows a weak inverse correlation (R = -0.23) with infrasound energy, while (b) bulk effusion rate shows a robust positive correlation (R = 0.74)

with frequency index for the same data. Data are color-coded based on source back-azimuths from Fig. 4 (orange=spillway, blue=transition, black=vent). Data range shown is from July 14 21:33:50 to July 15 01:53:30 UTC, although gaps in the effusion rate data occur in the final hour

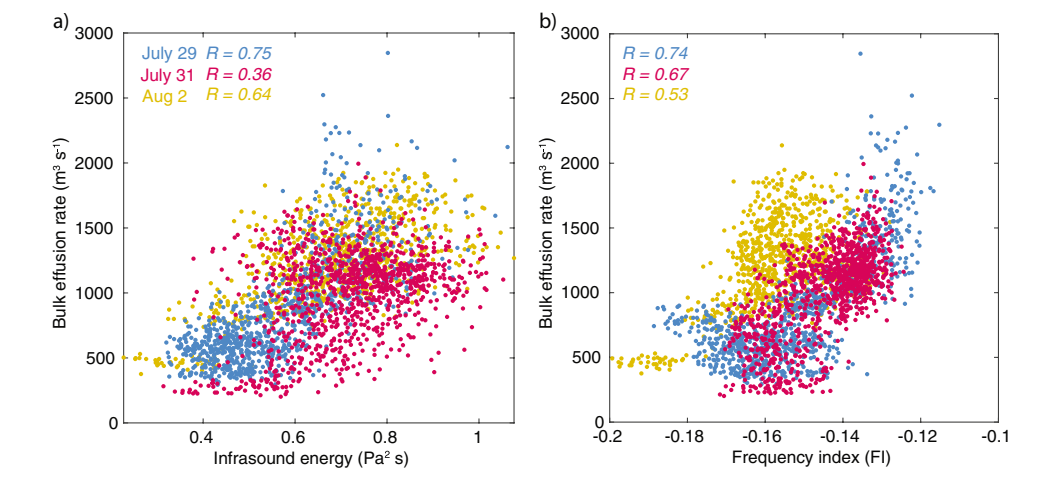


**Fig. 7** Lava effusion rate compared with infrasound energy and frequency index during three surges in effusion rate. Bulk effusion rate data from Patrick et al. (2019). (a) Bulk effusion rate shows moderate to strong correlation with infrasound energy during the July 29

(blue) and Aug 2 (yellow) surges but a weak correlation for the July 31 (red) surge. (b) Bulk effusion rate shows a moderate to strong correlation with infrasound frequency index for all three surges, and a better average correlation than infrasound energy

thus a better average correlation than energy (Fig. 7). Patrick et al. (2019) presented a similar correlation between effusion rate, infrasound energy, and RSAM, and noted that the surge increases in effusion rate followed collapses 40 km away at Kīlauea's summit. Effusion rates increased at fissure 8 only minutes after summit collapses, indicating connectivity between the summit and fissure 8 and suggesting that the collapses generated increased pressure in the plumbing system that raised the effusion rate for hours following collapses (Patrick et al. 2019). The surge events near the end of the eruption produced shifts in back-azimuth toward the spillway for 2–4 h before slowly returning to the

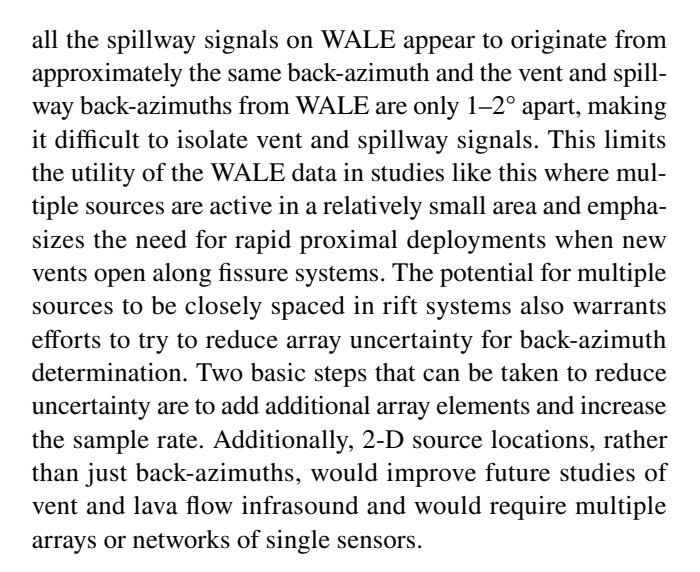
vent back-azimuth, but most of the source back-azimuths pointed toward the vent – transition area with few spillway back-azimuths. The July 29 surge shows the clearest correlation between back-azimuth, FI, and effusion rate, while the July 29 and July 31 back-azimuths are dominated by vent locations with lesser numbers of transition locations. Field observations and UAS videos show supercritical flow features similar to those observed during the pulse events. However, vigorous degassing continued and often increased at the vent throughout surges, unlike during pulses when vent activity waned as spillway activity increased (Patrick et al. 2019). We attribute the lack of spillway back-azimuths



during surges to the vent remaining the dominant infrasound source. Despite the lack of spillway sources indicated by the array processing, we interpret the maintained correlation between bulk effusion rate and FI as evidence that supercritical flow was producing lava flow infrasound in the spillway that contributed substantially to the overall frequency content of the surge signals. The algorithm we use to determine back-azimuths results in a single back-azimuth value per window of data and favors more energetic sources over weaker sources, although the infrasound signal comprises contributions from all active sources. Other beamforming algorithms are capable of resolving multiple sources in the same window of data and could be explored in future work to better resolve the temporal evolution of coeval vent and spillway sources (den Ouden et al. 2020).

Infrasound FI appears to be a useful proxy for tracking significant changes in bulk effusion rate in the fissure 8 pulse and surge data. Pulse and surge events resulted in large variations in bulk effusion rate, but on very different timescales and with different distal effects. The pulse events produced essentially no change in flow downstream of the spillway, suggesting no change to dense rock equivalent (DRE) effusion rate because the spillway bulk effusion rate was controlled solely by variations in the gas content of the lava (Patrick et al. 2019). The surges did result in downstream changes to flow with overflows and breakouts observed kilometers away from the vent, indicative of a significant increase in DRE effusion rate (Patrick et al. 2019). Hazards from increased effusion rate were associated with both pulses and surges. The pulse hazards were largely confined to channel overflows within ~ 1 km of the vent, while the surge hazards extended many kilometers from the vent (Patrick et al. 2019). In both cases, the infrasound FI provides information about the velocity of the flow proximal to the vent, and thus effusion rate. In the special case of the fissure 8 pulses and surges, infrasound energy (or amplitude) and event duration provide additional information about where to expect changing hazard conditions. An advantage of the infrasound FI over either seismic or infrasound amplitude methods is that it is capable of discriminating vent activity from supercritical flow activity, and thus can distinguish between degassing sources and high-speed flow sources.

The infrasound data analyzed here were recorded on an array just 500 m from the vent with good azimuthal separation between the vent and spillway. Data from a permanent infrasound array (WALE) operated by the U.S. Geological Survey's Hawaiian Volcano Observatory and installed during the LERZ eruption in 2018 shows variations in amplitude and back-azimuth during pulse events similar to the FIS8 data (Fig. 2 in Online Resource 2). However, the WALE array is ~ 3.7 km from fissure 8 and located further north than the FIS8 campaign array with respect to the fissure 8 vent and spillway (Fig. 1 in Online Resource 2). Thus,



# **Conclusions**

Kīlauea's 2018 fissure 8 eruption generated abundant infrasound that was recorded on a campaign array located near the vent and lava flow spillway. Large variations in bulk effusion rate occurred on both short (6-10-min pulses) and long (hours-long surges) timescales. During high flow rates, velocities of 10-17 m s<sup>-1</sup> were observed by UAS and ground-based observations. These high flow velocities resulted in supercritical flow in the spillway and produced lateral breaking waves, bow shocks, and other flow features associated with supercritical flow in fluvial systems. Spectral analysis of infrasound originating from the vent and spillway reveals differences in the source characteristics. We use the infrasound frequency index (FI) to distinguish vent and spillway source contributions. The lava flow critical state, or Froude value (Fr), was derived from UAS videos and shows a positive correlation with infrasound FI. We suggest that the spillway infrasound source was produced by fluid - air interactions during times when breaking waves were occurring in the flow. The infrasound FI values show a positive correlation with bulk effusion rate for both pulse and surge events and provide a simple method of distinguishing a vent or degassing source from a high-speed flow source. Our results indicate that infrasound offers a new way to characterize lava flow channel hydraulics and is a powerful tool for monitoring effusive eruptions when high-speed flows are possible. Future work relating infrasound to lava flow and other fluvial processes will provide insight on the precise source mechanisms and potentially allow infrasound-derived flow parameters.

**Supplementary Information** The online version contains supplementary material available at https://doi.org/10.1007/s00445-021-01488-7.



Bulletin of Volcanology (2021) 83:66 Page 11 of 12 66

Acknowledgements We thank the staff of the U.S. Geological Survey (USGS) Hawaiian Volcano Observatory, the USGS-DOI UAS Kīlauea Response Team, Hawai'i County Civil Defense, the USGS Volcano Science Center staff, University of Hawai'i at Hilo, the Federal Emergency Management Agency, and other partner agencies, scientific colleagues, and residents who supported data collection, processing, and analysis during the eruption response. Careful reviews by Oliver Lamb, Silvio De Angelis, and Arthur Jolly improved the paper. Infrasound data are available through the IRIS Data Management Center. D. Fee acknowledges funding from NSF Grant EAR-1901614. Any use of trade, firm, or product names is for descriptive purposes only and does not imply endorsement by the U.S. Government.

# References

- Allstadt KE, Matoza RS, Lockhart AB et al (2018) Seismic and acoustic signatures of surficial mass movements at volcanoes. J Volcanol Geotherm Res 364:76–106. https://doi.org/10.1016/j.jvolgeores.2018.09.007
- Arrowsmith SJ, Hedlin MAH (2005) Observations of infrasound from surf in southern California. Geophys Res Lett 32:L09810. https:// doi.org/10.1029/2005GL022761
- Aucan J, Fee D, Garcés M (2006) Infrasonic estimation of surf period. Geophys Res Lett 33:L05612. https://doi.org/10.1029/2005G L025086
- Baloga S, Spudis PD, Guest JE (1995) The dynamics of rapidly emplaced terrestrial lava flows and implications for planetary volcanism. J Geophys Res 100(B12):24509–24519. https://doi. org/10.1029/95JB02844
- Buurman H, West ME (2010) Seismic precursors to volcanic explosions during the 2006 eruption of Augustine Volcano, chapter 2 of Power, JA, Coombs, ML, Freymueller, JT,eds, 2006 Erupt Augustine Volcano, Alaska U.S. Geol. Sur. Prof Pap 1769 41–57. https://doi.org/10.3133/pp17692
- Chanson H (2009) Current knowledge in hydraulic jumps and related phenomena. A survey of experimental results. Eur J Mech B/fluids 28:191–210. https://doi.org/10.1016/j.euromechflu.2008.06.004
- Chow VT (1959) Open-channel hydraulics. McGraw-Hil, McGraw-Hill, New York
- den Ouden OFC, Assink JD, Smets PSM et al (2020) CLEAN beamforming for the enhanced detection of multiple infrasonic sources. Geophys J Int 221:305–317. https://doi.org/10.1093/gji/ggaa010
- Desmither LG, Diefenbach AK, Dietterich HR (2021) Unoccupied Aircraft Systems (UAS) video of the 2018 lower East Rift Zone eruption of Kīlauea Volcano, Hawaii . US Geol Surv
- Dietterich HR, Diefenbach AK, Soule SA et al (2021) Lava effusion rate evolution and erupted volume during the 2018 Kīlauea lower East Rift Zone eruption. Bull Volcanol 83:25. https://doi.org/10.1007/s00445-021-01443-6
- Fee D, Garces M, Orr T, Poland M (2011) Infrasound from the 2007 fissure eruptions of Kīlauea Volcano. Hawai'i 38:1–5. https://doi.org/10.1029/2010GL046422
- Fee D, Lyons J, Haney M et al (2020) Seismo-acoustic evidence for vent drying during shallow submarine eruptions at Bogoslof volcano, Alaska. Bull Volcanol 82:2. https://doi.org/10.1007/ s00445-019-1326-5
- Fee D, McNutt SR, Lopez TM et al (2013) Combining local and remote infrasound recordings from the 2009 Redoubt Volcano eruption. J Volcanol Geotherm Res 259:100–114. https://doi.org/10.1016/j. jvolgeores.2011.09.012

- Gansecki C, Lopaka Lee R, Shea T, et al (2019) The tangled tale of Kīlauea's 2018 eruption as told by geochemical monitoring. Science (80) 366: https://doi.org/10.1126/science.aaz0147
- Garcés M, Harris A, Hetzer C, et al (2003a) Infrasonic tremor observed at Kilauea Volcano, Hawai'i. Geophys Res Lett 30, 2023, doi:https://doi.org/10.1029/2003GL018038, 20.
- Garcés M, Hetzer C, Merrifield M et al (2003b) Observations of surf infrasound in Hawai'i. Geophys Res Lett 30:2264. https://doi.org/ 10.1029/2003GL018614
- Geist DJ, Harpp KS, Naumann TR et al (2008) The 2005 eruption of Sierra Negra volcano, Galápagos, Ecuador. Bull Volcanol 70:655–673. https://doi.org/10.1007/s00445-007-0160-3
- Griffiths RW (2000) The dynamics of lava flows. Annu Rev Fluid Mech 32:477–518. https://doi.org/10.1146/annurev.fluid.32.1.477
- Harris AJL, Baloga SM (2009) Lava discharge rates from satellitemeasured heat flux. Geophys Res Lett 36:1–5. https://doi.org/10. 1029/2009GL039717
- Jeffreys H (1925) The flow of water in an inclined channel of rectangular section. London, Edinburgh, Dublin Philos Mag J Sci 49:793–807. https://doi.org/10.1080/14786442508634662
- Johnson JB, Palma JL (2015) Lahar infrasound associated with Volcán Villarrica's 3 March 2015 eruption. Geophys Res Lett 42:6324– 6331. https://doi.org/10.1002/2015GL065024
- Le Moigne Y, Zurek JM, Williams-Jones G, et al (2020) Standing waves in high speed lava channels: a tool for constraining lava dynamics and eruptive parameters. J Volcanol Geotherm Res 401:. https://doi.org/10.1016/j.jvolgeores.2020.106944
- Lipman P, Banks N (1987) A'a flow dynamics, 1984 Mauna Loa eruption. USGS Prof Pap 1350:1527–1567
- Lyons JJ, Haney MM, Fee D, Paskievitch JF (2014) Distinguishing high surf from volcanic long-period earthquakes. Geophys Res Lett 41:1171–1178
- Marchetti E, Ripepe M, Ulivieri G, Kogelnig A (2015) Infrasound array criteria for automatic detection and front velocity estimation of snow avalanches: towards a real-time early-warning system. Nat Hazards Earth Syst Sci 15:2545–2555. https://doi.org/10.5194/nhess-15-2545-2015
- Marchetti E, Walter F, Barfucci G et al (2019) Infrasound array analysis of debris flow activity and implication for early warning. J Geophys Res Earth Surf 124:567–587. https://doi.org/10.1029/2018JF004785
- Matoza RS, Fee D, Garcés MA (2010) Infrasonic tremor wavefield of the Pu`u `Ō̄o; crater complex and lava tube system, Hawaii, in April 2007. J Geophys Res 115:B12312. https://doi.org/10.1029/2009jb007192
- Matoza RS, Fee D, Neilsen TB et al (2013) Aeroacoustics of volcanic jets: acoustic power estimation and jet velocity dependence. J Geophys Res Solid Earth 118:6269–6284. https://doi.org/10.1002/ 2013JB010303
- Neal CA, Brantley SR, Antolik L et al (2019) The 2018 rift eruption and summit collapse of Kīlauea Volcano. Science 80(363):367–374
- Olson JV, Szuberla CAL (2005) Distribution of wave packet sizes in microbarom wave trains observed in Alaska. J Acoust Soc Am 117:1032–1037. https://doi.org/10.1121/1.1854651
- Patrick MR, Dietterich HR, Lyons JJ et al (2019) Cyclic lava effusion during the 2018 eruption of Kīlauea Volcano. Science (80) 366:aay9070. https://doi.org/10.1126/science.aay9070
- Ripepe M, De Angelis S, Lacanna G, Voight B (2010) Observation of infrasonic and gravity waves at Soufriere Hills Volcano, Montserrat. Geophys Res Lett 37:1–5. https://doi.org/10.1029/2010G L042557
- Ronan TJ, Lees JM, Mikesell TD et al (2017) Acoustic and seismic fields of hydraulic jumps at varying Froude numbers. Geophys Res Lett 44:9734–9741. https://doi.org/10.1002/2017GL074511



66 Page 12 of 12 Bulletin of Volcanology (2021) 83:66

Schimmel A, Hübl J (2016) Automatic detection of debris flows and debris floods based on a combination of infrasound and seismic signals. Landslides 13:1181–1196. https://doi.org/10.1007/s10346-015-0640-z

- Schmandt B, Aster RC, Scherler D et al (2013) Multiple fluvial processes detected by riverside seismic and infrasound monitoring of a controlled flood in the Grand Canyon. Geophys Res Lett 40:4858–4863. https://doi.org/10.1002/grl.50953
- Slatcher N, James MR, Calvari S et al (2015) Quantifying effusion rates at active volcanoes through integrated time-lapse laser scanning and photography. Remote Sens 7:14967–14987. https://doi.org/10.3390/rs71114967
- Szuberla CAL, Olson JV (2004) Uncertainties associated with parameter estimation in atmospheric infrasound arrays. J Acoust Soc Am 115:253–258. https://doi.org/10.1121/1.1635407
- Tedesco D, Vaselli O, Papale P et al (2007) January 2002 volcanotectonic eruption of Nyiragongo volcano, Democratic Republic

- of Congo. J Geophys Res Solid Earth 112:1–12. https://doi.org/10.1029/2006JB004762
- Toney L, Fee D, Allstadt KE et al (2021) Reconstructing the dynamics of the highly similar May 2016 and June 2019 Iliamna Volcano (Alaska) ice-rock avalanches from seismoacoustic data. Earth Surf Dyn 9:271–293. https://doi.org/10.5194/esurf-9-271-2021
- Ulivieri G, Marchetti E, Ripepe M et al (2011) Monitoring snow avalanches in Northwestern Italian Alps using an infrasound array. Cold Reg Sci Technol 69:177–183. https://doi.org/10.1016/j.coldregions.2011.09.006
- Vicari A, Ganci G, Behncke B et al (2011) Near-real-time forecasting of lava flow hazards during the 12–13 January 2011 Etna eruption. Geophys Res Lett 38:1–7. https://doi.org/10.1029/2011GL047545
- Zoeller M, Patrick M, Neal C (2018) Crisis remote sensing during the 2018 lower east rift zone eruption of ki lauea volcano. Photogramm Eng Remote Sensing 84:749–751

